Journal of Dynamic Behavior of Materials (2019) 5:13–23
https://doi.org/10.1007/s40870-018-00180-w

Spall Characterization of EPON 828 Epoxy with Embedded Carbon Nanotubes

J. Huneault[1] · J. E. Pepper[2] · M. Rahmat[3] · B. Ashrafi[4] · O. E. Petel[2]

Received: 15 October 2018 / Accepted: 18 December 2018 / Published online: 3 January 2019

Abstract
The increasing use of polymer nanocomposites in armor applications requires an understanding of how these materials behave at strain-rates relevant to ballistic impacts. Of particular interest is the role of the microstructure on the failure of these materials under dynamic tensile loading. In the present study, plate impact experiments were conducted in order to measure the spall strength of a neat epoxy (EPON 828) and an epoxy–carbon nanotube composite. The addition of pristine carbon nanotubes (CNTs) to the epoxy resulted in a composite material with a lower spall strength than the neat epoxy matrix material. Recovered composite fragments were imaged with a scanning electron microscope. Instances of nanotube pull-out were identified on internal fracture surfaces. The lower spall threshold of the epoxy–CNT composite was attributed to the comparatively weak epoxy–CNT interface, which provides potential sites from which spall failure can favorably nucleate.

Keywords Spall · Epoxy composite · Carbon nanotube (CNT) · Fracture · Impact

Introduction

Polymer–matrix composites are an attractive option for ballistic armor applications due to their high mass-normalized stiffness, strength, and energy dissipation capabilities [1, 2]. As a result, the shock loading and ballistic response of conventional polymer–matrix composites, such as those in which woven glass or carbon fibers are embedded in an epoxy resin matrix, have been extensively studied [3–6]. In recent years, composite research has focused on the possibility of improving the mechanical properties of the epoxy matrix through the addition of nanomaterials [7, 8]. In particular, the high stiffness, strength, and ductility of carbon nanotubes (CNTs) have motivated the development of epoxy–CNT composites in which the nano-reinforcements are dispersed within the epoxy matrix [9, 10]. There is evidence of improvements in stiffness and strength with the addition of CNTs to a polymer matrix [10, 11], however issues related to uniform dispersion of the high-aspect-ratio CNTs and the weak nanotube–matrix interface have prevented these nanocomposites from achieving their theoretical potential.

While epoxy–CNT composites have been studied extensively under quasi-static loading conditions [7, 9, 12], the response of these materials at the elevated strain rates relevant to ballistic impact has not been widely examined [1, 2, 13]. Of particular interest is the response of these materials to spall, a typical failure mode in ballistic armour systems which occurs when an impact driven shock wave reflects from a free surface as an expansion front and interacts with the expansion front behind the shock to cause tensile failure. Spall is typically studied using plate impact experiments, where the impact of a flyer plate drives shock waves in the target and flyer which reflect from their respective free surfaces as expansion fronts that meet and cause tensile failure within the target [14]. Such experiments can achieve tensile strain rates in excess of 10^4/s with well-defined loading conditions, which allow the maximum tension in the material to be estimated from

✉ O. E. Petel
oren.petel@carleton.ca

J. Huneault
justin.huneault@mail.mcgill.ca

[1] Department of Mechanical Engineering, McGill University, Montreal, QC H3A 0C3, Canada

[2] Department of Mechanical and Aerospace Engineering, Carleton University, Ottawa, ON K1S 5B6, Canada

[3] Aerospace, National Research Council Canada, Ottawa, ON K1A 0R6, Canada

[4] Aerospace, National Research Council Canada, Montreal, QC H3T 2B2, Canada

the evolution in the free-surface velocity profile [14]. The measured spall strength in plate impact experiments refers to the maximum tension supported by the target material prior to the relief of tensile stresses due to the nucleation and growth of voids or cracks, which occur at the initiation of spall fracture. The effect of loading conditions (strain rate, pressure pulse amplitude, and pulse duration) on the spall strength and fracture modes inferred from recovered targets, can be used to develop a fundamental understanding of how these materials fail at strain rates relevant to ballistic impact.

A number of studies have examined the spall response of neat polymer materials and polymer–matrix composites. Curran et al. studied spall failure in polycarbonate [15], while Golubev et al. studied the effect of temperature on the spall strength of a variety of polymers [16]. Pepper et al. examined the effect of resin curing agent on the spall strength of EPON 828 epoxy [17]. Dandekar et al. [4] and Yuan et al. [18] measured the delamination strength of glass–fiber-reinforced polymer composites using planar and oblique plate impacts. Zaretsky et al. compared the spall strength of layered glass–fiber-reinforced composites with that of the neat epoxy matrix and found a reduction in strength from 240 to 160 MPa with the addition of the glass fibers [5]. Katz et al. studied the effect of varying the fiber type and surface treatment on the spall strength of laminated epoxy composites [19]. The addition of fibers had a significant effect on spall strength, with Kevlar fibers strengthening the system and Spectra fibers leading to a lowering of the spall strength [19]. The difference in behavior was attributed to the presence of residual compressive stresses in the Kevlar fiber composite [19]. Bie et al. studied the effect of adding dispersed CNTs to an epoxy matrix and found that the spall strength of the material was unaffected by the addition of the nanotubes [13]. Imaging of fracture surfaces on impacted samples showed failure modes that are commonly observed in quasi-static experiments: fiber pull-out, sliding, and breaking [13].

Although it is well understood that particle inclusions and second-phase intermetallics in metals act as nucleation sites for spall failure [14, 20–22], the effect of fiber inclusions on the spall strength of polymer–matrix nanocomposites has not been widely studied. While the addition of nano-reinforcements has the potential to improve material strength and fracture toughness, the particles or tubes may act as nucleation sites for spallation at high strain rates. This paper will present spall strength measurements obtained via plate impact experiments performed on dispersed CNT polymer–matrix composites and samples of the neat epoxy matrix. The dependence of the spall strength on the strain rate and incident pressure pulse will be examined in both the neat and nanocomposite epoxy through a variation in the flyer material and its impact velocity.

Materials and Methods

Material Preparation

EPON 828, a bisphenol-A epoxy resin cured with EPIKURE 3223 was chosen as the matrix material for this study. The resin and curing agent were sourced from Hexion Inc. The neat epoxy samples, identified as EPON 828-A, were fabricated with a resin-to-curing agent mix ratio of 100:12 by weight. The epoxy was prepared by mixing the resin and curing agent with a planetary mixer for 2 min at 2000 rpm. The mixture was then degassed under vacuum and poured into open moulds. The specimens were left to cure at room temperature for two days, the first 8 h of which was inside an autoclave with a minimum pressure of 5.9 bar. Once cured, the specimens were removed from their moulds and then post-cured at 120 °C for 2 h. Finally, rough edges and excess material were removed by wet polishing with sandpaper (500 grit).

The epoxy–CNT composite, identified as EPON 828-A + CNT, was composed of the EPON 828 epoxy matrix mixed with pristine NC7000™ industrial-grade multi-walled carbon nanotubes supplied by Nanocyl SA. The nanotubes were produced via a catalytic chemical vapor deposition technique, resulting in a carbon purity of 90%, an average tube length of 1.5 μm, an average diameter of 9.5 nm, and a density of 1.7 g/cm^3 according to manufacturer specifications. The composite was created by integrating the required quantity of dry nanotubes into EPON 828 resin with a planetary mixer for three, 3 min cycles at 2000 rpm. After integration, the EPIKURE 3223 curing agent was added at a resin-to-curing agent weight ratio of 100:12 and mixed for 2 min. The composite specimens were prepared using the same degassing, curing, and post-curing procedures as the neat epoxy samples. The final composite contained 1 wt% CNT. As with the neat epoxy specimens, any rough edges on the composite specimens were removed by wet polishing with sandpaper (500 grit).

Plate Impact Experimental Arrangement

Spall experiments were performed using a 64-mm-diameter (d) gas-gun to launch thin flyer plates onto the target samples at velocities ranging from approximately 220–730 ms^{-1}. A schematic of the experimental assembly can be seen in Fig. 1. The flyer plates, which had thicknesses (w_f) ranging from 1.6 to 2.0 mm, were glued to a plastic (nylon or PVC) sabot such that they have an unsupported rear free surface. Aluminum 6061-T6 and PMMA flyers were launched onto epoxy targets with thicknesses

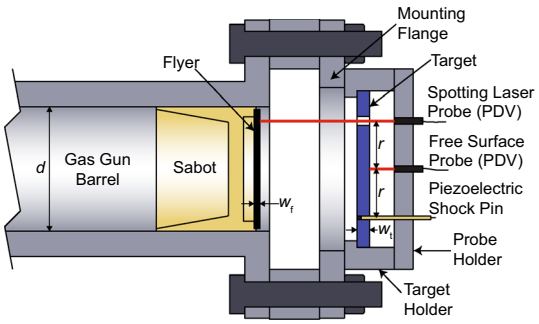

Fig. 1 Labeled schematic of the plate impact experimental arrangement

Table 1 The acoustic properties of flyer and target materials for the plate impact experiments

Material	ρ_0 (g/cm^3)	C_B (km/s)	C_L (km/s)
Aluminum 6061-T6	2.70[a]	5.27[a]	6.40[a]
PMMA	1.19[b]	2.23[b]	2.69[b]
EPON 828-A	1.185[b]	2.26[b]	2.64[b]
EPON 828-A + CNT	1.189[c]	2.26[b]	2.64[b]

[a]Marsh [23]

[b]Carter and Marsh [24]

[c]Determined from ideal solution mixture rules

(w_t) ranging from approximately 3.0–6.6 mm. The target thickness was made sufficiently small as to ensure that the expansion front from the edge of the sample did not reach the central axis in time to interfere with the spall measurement, thus ensuring that the strain remained one-dimensional. The use of both aluminum and PMMA flyers allowed for a variation in the shape and amplitude of the loading pulses due to the differences in the speed of sound and shock impedance (density multiplied by wave velocity) of both materials. The close impedance match between PMMA flyers and the epoxy targets provided a nearly symmetric impact, while aluminum flyers generated greater shock stresses upon impact due to their comparatively high speed of sound and density. The choice was made to use PMMA rather than epoxy as the flyer material for symmetric impacts due to the widespread availability of readily cut PMMA sheet. Table 1 summarizes the relevant acoustic properties of the aluminum and PMMA flyers as well as the epoxy targets. It was assumed that the addition of 1 wt% CNT to the epoxy had a negligible effect on the acoustic wave speeds.

The spall strength was determined by measuring the evolution of the rear surface velocity using a photonic Doppler velocimetry (PDV) system [25] coupled to a 40 GHz sampling rate digitizer, allowing for ≈ 2 m/s accuracy at a time resolution of 20 ns. The PDV system, which measures

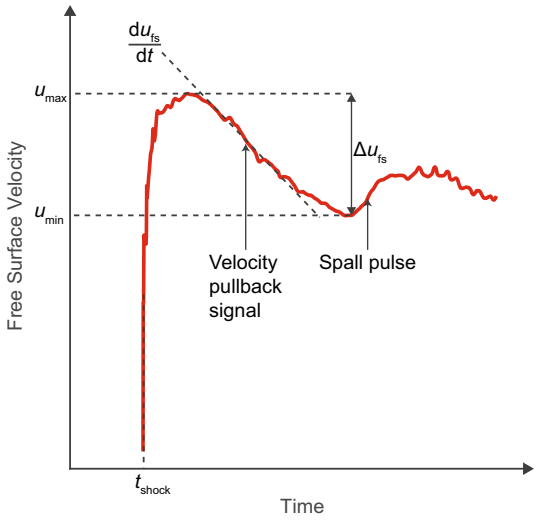

Fig. 2 Labeled graph of the free-surface velocity evolution as a function of time for a plate impact experiment

material velocity based on the magnitude of the Doppler shift in a laser signal reflected from a moving surface, requires that the free surface of the epoxy samples be coated with a material that is reflective to the 1550 nm infrared laser. Earlier experiments, performed on the neat epoxy samples, used physical vapor deposition to coat the back surface of the samples with a 40–60 nm layer of aluminum. The roughness of the rear surface lead to significant ejecta [17] that partially obscured the free surface and increased the noise in the PDV data. Therefore, in the present study involving epoxy–CNT composite targets, an infrared reflective surface was obtained by adhering a 0.05 mm thick aluminized Mylar sheet to the rear surface. The impact velocity (v_i) of the flyer plate was measured using a second PDV probe (identified as the spotting laser probe) projected through a 4.8 mm diameter hole located 25.4 mm away from the central axis of the target. A piezoelectric shock pin (CA-1135 from Dynasen Inc.) located 25.4 mm from the central axis opposite to the spotting laser probe was used to trigger the diagnostics. The gas gun barrel and target chamber were flushed with helium and vacuumed in order to minimize gas cushion effects. The test section pressure for Shots 1–5 was in the range of 5–8 Torr, and was reduced to approximately 1 Torr for subsequent shots following improvements to the vacuum system.

Plate Impact Analysis Methods

The time evolution of the target free-surface velocity, for a typical spall experiment, is shown in Fig. 2, where the main features of the signal have been labeled. The arrival of the impact driven shock wave at the free surface leads to a nearly instantaneous increase in the free-surface velocity that is proportional to the shock stress. The shock wave reflects as

an expansion front that interacts with the expansion front originating from the flyer free surface, which generates tensile stresses in the target and leads to a gradual decline in the free-surface velocity. The slope of this velocity pullback signal is proportional to the tensile strain rate in the target. If the tensile stresses are sufficient to spall the target material, a compressive wave front is formed by the relaxation of the tensile stress during fracture. Upon reaching the free surface, this compressive wave front, referred to as a spall pulse, leads to an increase in the free-surface velocity which indicates the onset of spall failure. The particle velocity behind the shock wave (u_p) as it reaches the free surface and the magnitude of the shock stress (σ_H) corresponding to the post-shock Hugoniot state in the target are given by [26]

$$u_p = \frac{1}{2} u_{max}, \tag{1}$$

$$\sigma_H = \rho_0 U_s u_p, \tag{2}$$

where u_{max} is the maximum post-shock velocity of the free surface of the target and ρ_0 is the initial density of the target material. Studies on the shock response of EPON 828 epoxy have demonstrated a linear relationship between particle velocity (u_p) and shock velocity (U_s) over the range of shock velocities probed in this study [24, 27]. The addition of 1 wt% CNT to the epoxy is not expected to have a significant effect on the $U_s - u_p$ relationship [28]. The shock velocity can then be obtained by the following empirical relation [27].

$$U_s = 2.64 + 1.66 u_p, \tag{3}$$

The tensile strain rate ($\dot{\epsilon}$) in the target material prior to spall can be determined by

$$\dot{\epsilon} \approx -\frac{1}{2C_B} \frac{du_{fs}}{dt}, \tag{4}$$

where $\frac{du_{fs}}{dt}$ is obtained from the slope of the free-surface velocity pullback signal and C_B is the bulk sound speed of the target material. The spall strength (σ_{sp}) of the target material can be determined from the free-surface velocity profile using the acoustics approach provided by Stepanov [29] that gives the linear approximation [14]

$$\sigma_{sp} = \rho_0 C_L \Delta u_{fs} \frac{1}{1 + \frac{C_L}{C_B}}, \tag{5}$$

where Δu_{fs} is the difference between the maximum free-surface velocity after the arrival of the shock (u_{max}) and the minimum free surface velocity prior to the arrival of the spall pulse (u_{min}), and C_L is the longitudinal sound speed.

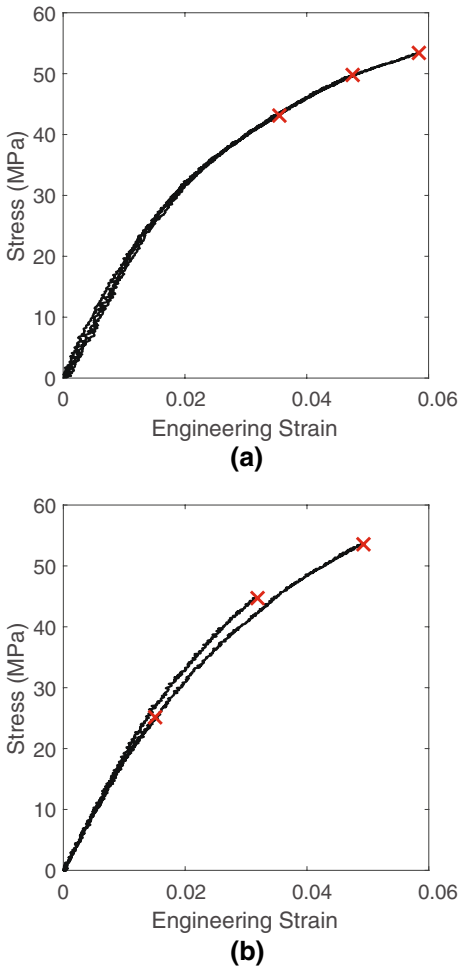

Fig. 3 Representative stress–strain curves for **a** the neat EPON 828-A epoxy and **b** EPON 828-A + CNT samples, obtained from uniaxial tensile tests

Results

Quasi-static Material Characterization

Quasi-static tensile tests were performed on neat epoxy and epoxy–CNT composite samples using a Fullam Substage load frame in order to characterize the materials. The tensile tests were conducted with dogbone specimens according to ISO 527-2 (Type 1BB), where samples with a gauge length of 12.0 mm were loaded with a displacement rate of 2 mm/min. Tension measurements were taken with a 45 N load cell having a resolution of 0.01 N, while elongation was obtained using a linear variable displacement transformer sensor with a resolution of 1 µm. The ultimate tensile strength (σ_{max}) and elongation at break (ϵ_{max}) for the series of tests performed on neat epoxy and epoxy–CNT composite samples are presented in Table 2, while representative stress–strain curves for the two materials are presented in Fig. 3. The 95%

Table 2 Epoxy material properties obtained from quasi-static uniaxial tensile tests

Sample	EPON 828-A		EPON 828-A + CNT	
	σ_{max} (MPa)	ϵ_{max}	σ_{max} (MPa)	ϵ_{max}
1	49.8	0.048	53.6	0.050
2	53.4	0.058	53.0	0.042
3	49.1	0.046	44.7	0.032
4	50.0	0.050	25.1	0.015
5	43.1	0.036	–	–
Mean	49.1	0.047	44.1	0.035
± (95%)	4.6	0.010	21.1	0.024

Table 3 Epoxy fracture toughness measurements obtained from quasi-static tests

Sample	EPON 828-A K_c (MPa/m$^{0.5}$)	EPON 828-A + CNT K_c (MPa/m$^{0.5}$)
1	1.29	1.31
2	0.94	1.40
3	1.10	1.36
4	1.14	1.37
5	0.76	1.28
Mean	1.05	1.34
± (95%)	0.25	0.06

confidence interval (T-distribution) on the mean of the ultimate tensile strength and elongation at break is also shown in Table 2. The epoxy–CNT data had greater variability, including one outlier (sample 4) which failed at a very low stress level. Otherwise, the ultimate tensile strength and elongation at break appear to be slightly reduced by the addition of the CNTs. The stress–strain curves of both materials showed a similar material response, including a non-linear elastic region with comparable stiffness, and sudden failure prior to necking.

Plane-strain fracture toughness (K_c) measurements were also taken for both materials under quasi-static conditions. Rectangular specimens (2 mm by 4 mm by 20 mm) were prepared in a Teflon mould. A precision saw was used to create a notch on the samples. The notch was then sharpened with a razor blade. Preparation of the notches and testing were conducted according to ASTM D5045 with a displacement rate of 3 mm/min. The results of the fracture toughness tests, which are presented in Table 3, show that the addition of CNTs increases the fracture toughness of the material by approximately 28%.

Plate Impact Experiments

The test parameters and results from 15 plate impact experiments performed on the neat epoxy and epoxy–CNT composite targets are presented in Table 4.[1] The free-surface velocity histories for the experiments are presented in Fig. 4. The time axis has been arbitrarily offset in order to present the data from all experiments on the same plot. The traces are numbered and colour-coded as a function of flyer and target material. A spall event was recorded in every experiment

Table 4 Overview of the experimental parameters and results for the plate impact experiments

Shot #	Target	w_t (mm)	Flyer plate	w_f (mm)	v_i (ms^{-1})	σ_{sp} (MPa)	$\dot{\epsilon}$ (10^4/s)	u_{max} (ms^{-1})	σ_H (GPa)
1	EPON 828-A	6.27	Al 6061	2.0	715	542	8.1	1109	2.34
2	EPON 828-A	6.43	Al 6061	2.0	671	529	6.4	1023	2.11
3	EPON 828-A	6.58	Al 6061	2.0	503	485	4.4	771	1.50
4	EPON 828-A	5.38	Al 6061	2.0	363	412	3.6	561	1.03
5	EPON 828-A	6.50	Al 6061	2.0	219	374	1.6	345	0.60
6	EPON 828-A + CNT	5.08	Al 6061	2.0	617	314	8.7	872	1.74
7	EPON 828-A + CNT	5.21	PMMA	1.6	625	327	7.5	592	1.10
8	EPON 828-A + CNT	4.57	PMMA	1.6	499	310	8.1	496	0.90
9	EPON 828-A + CNT	3.02	PMMA	1.6	355	275	8.5	350	0.61
10	EPON 828-A + CNT	6.35	Al 6061	2.0	612	283	7.0	814	1.60
11	EPON 828-A + CNT	6.31	Al 6061	2.0	675	327	4.3	844	1.68
12	EPON 828-A + CNT	6.27	Al 6061	2.0	347	309	2.4	454	0.81
13	EPON 828-A + CNT	6.21	PMMA	1.6	496	234	4.9	407	0.72
14	EPON 828-A + CNT	6.15	PMMA	1.6	636	268	5.2	472	0.85
15	EPON 828-A + CNT	5.81	PMMA	1.6	730	305	6.9	647	1.22

[1] The experiments performed on neat EPON 828 targets were reported in a previous study [17], but are presented in this work as additional analysis has been performed on the data and they are essential to the comparison with the epoxy–CNT composite samples.

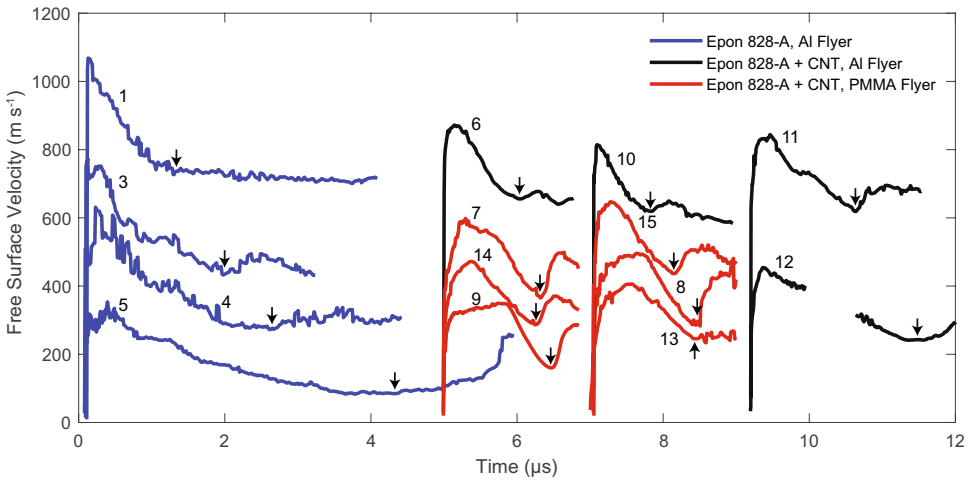

Fig. 4 Measured free-surface velocity as a function of time for the plate impact experiments. The time axis has been arbitrarily shifted to show all experiments on the same graph. The curves are color coded as a function of target and flyer material. Arrows indicate the arrival of the spall pulse. (Color figure online)

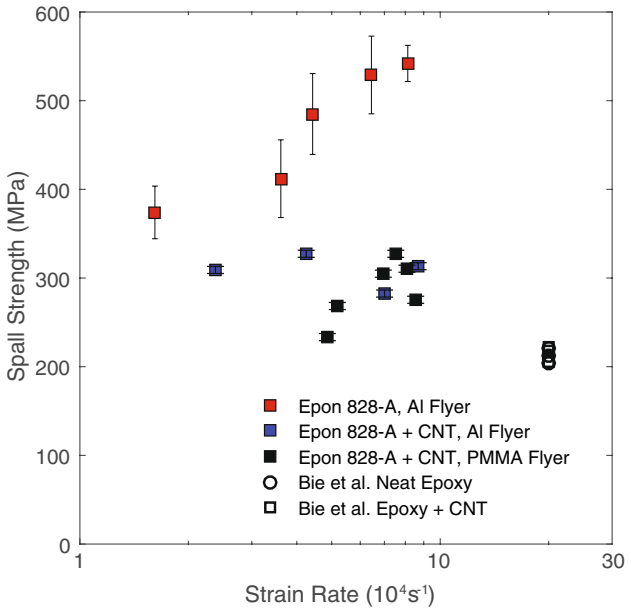

Fig. 5 Measured spall strength as a function of strain rate for the plate impact experiments. Data from Bie et al. is also shown for comparison [13]

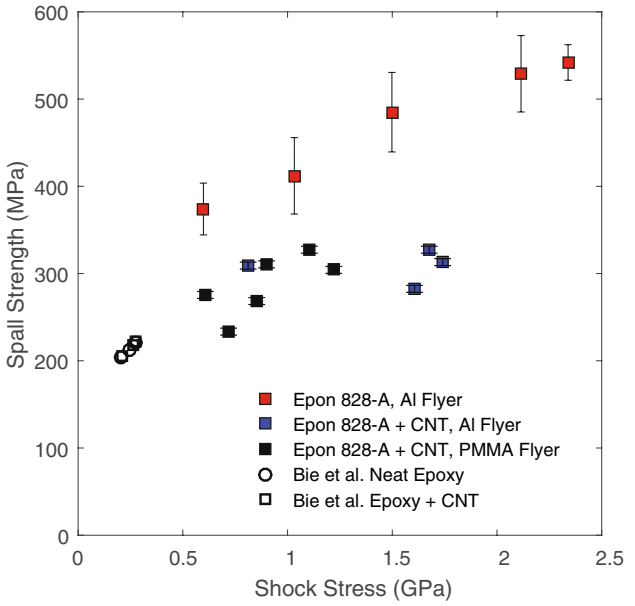

Fig. 6 Measured spall strength as a function of the shock stress for the plate impact experiments. Data from Bie et al. is also shown for comparison [13]

and is identified by an arrow in Fig. 4. Shot 2 has been omitted as it directly overlaps with Shot 1. The interruption of the Shot 12 trace was due to the voltage going off-scale on the digitizer.

The spall strength obtained from the free-surface velocity traces is plotted as a function of strain rate in Fig. 5 and peak stress prior to unloading in Fig. 6. Data from plate impact experiments performed by Bie et al. [13] on a bisphenol-A epoxy system, which was tested as a neat epoxy and with pristine 1 wt% multi-walled CNTs dispersed within the matrix, has also been included for comparison.[2] The variation in the strain rate and shock pressure was achieved by varying the impact velocity and flyer material: increasing the impact velocity resulted in a greater strain rates and shock stress, while aluminum flyer plates generated greater shock stresses than PMMA flyers at equivalent impact velocities.

[2] The neat epoxy had an ultimate tensile strength of 73MPa, an elongation to failure of 0.029, and a fracture toughness of 0.46 MPa/m$^{0.5}$, while the epoxy–CTN composite had an ultimate tensile strength of 66MPa, an elongation to failure of 0.026, and a fracture toughness of 0.60 MPa/m$^{0.5}$ [7].

The neat EPON 828 samples exhibited a higher spall strength (374–542 MPa) than the EPON 828–CNT composites (234–327 MPa) over the range of tested strain rates and shock stresses. The neat epoxy showed an increase in spall strength with increasing shock stress and strain rate, while the epoxy–CNT samples did not show an obvious correlation between spall strength and strain rate or shock stress. The velocity measurement error of the PDV system should result in an uncertainty of ± 4 MPa in the calculated spall strength. However, the highly dynamic behavior of free-surface velocity traces in spall experiments means that a loss of signal quality near the maximum or minimum velocity (u_{max} or u_{min}) can significantly increase the measurement uncertainty. Ejecta of the aluminum coating on the neat EPON 828 samples [17] partially obstructed the PDV signal which resulted in uncharacteristically noisy free-surface velocity traces and increased uncertainty in the spall strength measurements. Error bars based on PDV measurement uncertainty and estimates of the error range for noisy signals are included in Figs. 5 and 6.

Discussion

Effect of CNT Addition on Spall Strength

Quasi-static material testing of the epoxy systems studied in this paper showed that the addition of pristine CNTs to the epoxy resulted in a slight decrease in ultimate tensile strength and elongation to failure, but a 28% increase in fracture toughness. These results are consistent with those of Liu and Wagner [30] and Tang et al. [7], where the addition of 1 wt% pristine CNTs to epoxy systems resulted in a reduction in tensile strength and elongation to failure, as well as an increase in the fracture toughness or impact strength. The greater variability of the ultimate tensile strength and elongation to break that was observed for the epoxy–CNT material may be due to an increase in the porosity of the samples. The addition of CNTs to the uncured epoxy increased the viscosity of the mixture which lead to a greater likelihood of having trapped gas bubbles. The resulting voids act as stress concentrations from which failure can initiate in a tensile test. These coarsely distributed flaws are unlikely to affect the spall failure of the material, which initiates simultaneously from a large number of fracture sites.

Despite observed similarities in quasi-static properties of the neat and CNT-laden epoxies, the plate impact experiments presented above showed a significant reduction in measured spall strength with the addition of CNTs to the EPON 828 epoxy matrix over a wide range of strain rates and shock stresses. The effect of CNT addition on spall strength observed in this paper is consistent with previous studies examining the impact response of conventional epoxy–fiber laminate composites, where the measured spall strength was significantly lower than is typical of polymer materials [4, 5, 18]. The reduction in spall strength is typically attributed to weaknesses at the interface between the fibers and the matrix material [5]. Similarly, the lower spall strength of the composite samples in this work is believed to be due to the relatively weak epoxy–CNT interface [31] providing favorable nucleation sites for the initiation of spall fracture. The relationship between spall strength and availability of failure nucleation sites has been extensively studied. This is true for metals, where models [32, 33] and experiments [20, 34] have shown that spall strength can be lowered by the availability of preferential nucleation sites such as grain boundaries, second-phase particles, or inclusions. A scanning electron microscope (SEM) image of a recovered epoxy–CNT fracture surface is shown in Fig. 7, where a number of nanotube ends can be seen protruding from the fracture surface, which is indicative of a fiber pull-out failure mode caused by loss of adhesion at the epoxy–CNT interface [7]. While Fig. 7 provides some indication of weakness at the fiber–epoxy interface, the recovery of samples undergoing incipient spall would help to further corroborate the theory that the fibers act as favorable nucleation sites for fracture.

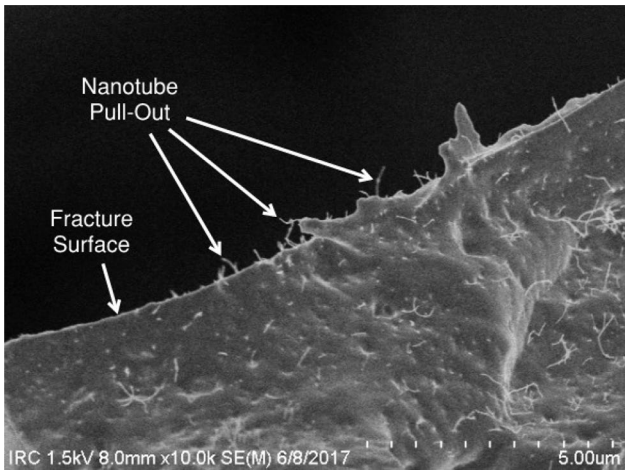

Fig. 7 Labeled SEM image of an internal fracture surface on a fragment of an epoxy–CNT composite

The findings discussed above do not agree with previously reported results from Bie et al. [13], where the spall strength of a similar epoxy system was found to be nominally unaffected by the addition of 1 wt% pristine CNTs. The difference in the observed relationship between CNT addition and spall strength may be explained by the fact that the experiments of Bie et al. [13] were carried out at lower levels of shock stress. From Fig. 6, it is apparent that the difference in the measured spall strength of the neat epoxy and epoxy–CNT is reduced as the shock stress is decreased. The difference in the effect of shock stress on the spall strength

for the neat epoxy and the epoxy–CNT composite observed in this work may be explained by the fact that the shock-induced compression collapses voids in the neat epoxy that would otherwise act as fracture nucleation sites, but does not suppress nucleation sites at the CNT–matrix interface of the composite material. It has been shown that flaws, such as micro-cracks and voids, can act as spall nucleation sites in polymers [15], and theorised that the shock stress may supress fracture nucleation sites in polymers [14] and liquids [35]. Therefore, it is possible that the observed difference in spall strength between the neat epoxy and epoxy–CNT composite can be attributed to suppression of nucleation sites in the neat epoxy, and that the strength of the two epoxies studied in this work would have been nearly equal at the shock stress levels studied by Bie et al. [13].

It is interesting to note that the results presented in this paper as well as those of the Bie et al. [13] study showed that the increase in quasi-static fracture toughness that resulted from CNT addition did not lead to an increase in spall strength of the epoxy systems. Grady [36] has developed a well-known model, supported by experimental evidence, which shows that spall strength can be correlated to fracture toughness in brittle spall, due to the increase in the energy required for crack propagation. Although elegant in its simplicity, the energy-based fracture model developed by Grady does not capture the entire nucleation, coalescence, and growth process of spall [14]. A particular limitation of correlating quasi-static properties to spall strength is the fact that spall may be strongly influenced by the nucleation and growth of a large number of micro-cracks that are generated during fracture [14], whereas quasi-static fracture toughness is measured by the growth of a single pre-existing flaw. The improvement in fracture toughness caused by the pullout, sliding, and breakage of CNTs at low strain rates [7], may not translate into spall strength improvements at high strain rates if either the initial crack nucleation and growth occurs within the epoxy matrix, or the fibers themselves act as nucleation sites for spall fracture. It should be noted that the results from this study focussed on the tension required for the onset of spall, and it is entirely possible that the greater fracture toughness of the epoxy–CNT composite could supress the late time damage evolution and fracture of the sample, such as spall scab formation, despite the reduction in spall strength.

Loading Profile Variation

The use of aluminum and PMMA flyers allowed for a significant variation in the shape and amplitude of the loading pulse applied to the epoxy targets. Figure 8 compares the position-time wave diagram for both types of flyers. The comparatively high speed of sound in the aluminum flyer plate creates a pressure pulse with a short plateau.

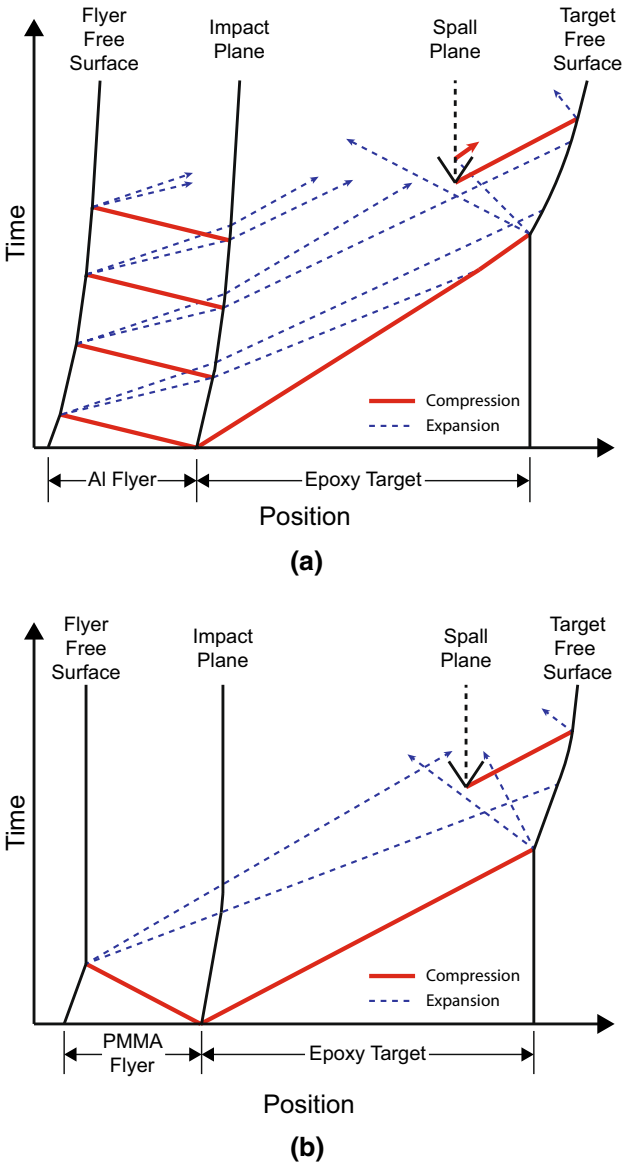

Fig. 8 Schematic wave diagram of the impact between **a** an aluminum flyer and an epoxy target and **b** a PMMA flyer and an epoxy target. Thick red lines indicate compression waves while thin blue lines indicate the head and tail of expansion fronts. (Color figure online)

For sufficiently high impact velocities, the expansion front originating from the back of the flyer catches up to the shock before reaching the epoxy free surface, thus forming a triangular pressure pulse (unsupported shock). PMMA flyers generate much longer pressure pulses that retain a square-top-like shape when they reach the free surface. The resulting pressure pulses for both aluminum and PMMA impacts are shown schematically in Fig. 9, where the spatial pressure distribution in the sample is shown for the incident pressure pulse (solid line) as well as after its reflection from the free surface (dashed line) but prior to spall. While the pressure

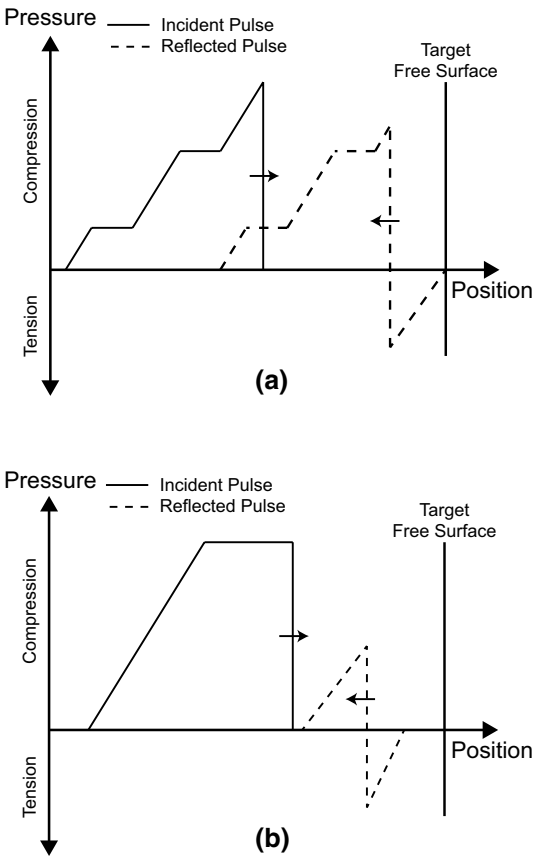

Fig. 9 Schematic of spatial distribution of the incident (solid line) and reflected (dashed line) pressure pulse that results from the impact between **a** an aluminum flyer and an epoxy target and **b** a PMMA flyer and an epoxy target

profile for a PMMA impact looks like a typical square pressure pulse, the impedance mismatch between the aluminum flyer and epoxy target leads to a step-wise decrease in the pressure behind the shock wave. The timescale of the step-wise profile is determined by the wave reverberation time across the flyer plate. Also of interest is the fact that for high velocity aluminum impacts, the unsupported shock causes the sample to be placed in tension as soon as the shock wave reflects from the free surface. For PMMA impacts, tension only accumulates in the target at a certain distance away from the free surface at a position that is determined by the duration of the square-top pressure pulse. The distance between the free surface and the plane where tension develops decreases for increasing ratios of target thickness to flyer thickness and for increasing impact velocities.

The features described above can be seen in the free-surface velocity traces of Fig. 4. In experiments performed at high impact velocities with aluminum flyers (e.g., Shots 1, 6, 10, and 11), the shock was directly followed by the expansion front as evidenced by the prompt velocity pull-back signal, whereas shots performed with PMMA flyers or aluminum flyers at lower velocities showed a distinct velocity plateau before the arrival of the expansion front. The effect of target thickness to flyer thickness ratio and shock stress on the shape of the pressure pulse is best observed with Shot 9, which had a particularly long ($\approx$ 1 μs) velocity plateau following the arrival of the shock due to the low sample thickness and impact velocity. The step-wise decrease in pressure behind the shock front produced by aluminum flyers manifested itself as short ($\approx$ 0.2 μs) velocity plateaus that interrupted the decay of the free-surface velocity. The plateaus were observed for a number of aluminum flyer experiments, particularly in the free-surface velocity histories from Shots 3, 5, and 11, but were not seen in the PMMA flyer experiments due to the close shock impedance match between the flyer and target material.

The free-surface velocity traces of Fig. 4 also show a relationship between the steepness of the spall pulse and the shape of the incident pressure pulse. Shots performed on both neat and CNT-modified samples with aluminum flyers (e.g., Shots 1, 3, 6, and 10) tended to have a spall pulse with a much slower rise time and lower amplitude than experiments with PMMA flyers (e.g., Shots 7, 8, and 9), the lone exception being Shot 13. The steepness of the spall pulse is known to be principally determined by the rate of damage evolution at the spall plane [37], with more rapid spall (larger number of nucleation sites and more rapid void growth) producing a steeper spall pulse [38]. Previous spall experiments performed on PMMA targets have shown a reduction in the steepness of the spall pulse with increasing shock stress amplitude [14], which was attributed to either increased crack tip plasticity [16] due to shock heating or suppression of nucleation sites (voids) during the initial shock loading [14]. In the experiments presented in this paper, the difference in spall pulse shape appears to be independent of shock stress, as can be seen by comparing low impact velocity aluminum flyer shots (e.g., Shots 3 and 4) to high impact velocity PMMA flyer shots (e.g., Shots 7 and 15) and is likely related to the effect of the pressure pulse shape. Spall studies performed on metal targets have shown that the shape and duration of the pressure pulse can have a significant effect on the level of spall damage as well as its location and extent within the sample [39, 40]. A wider extent of damage has been observed for triangular pressure pulses well above the spall threshold when compared to an equivalent square-top pressure pulse [39]. This is due to the fact that, as demonstrated in Fig. 9, triangular pressure pulses create a quasi-linearly increasing tension which extends from the free surface to the head of the expansion front, whereas square-top pulses lead to more localized damage at the plane where the two expansion fronts meet. The weaker spall pulse seen in the aluminum flyer experiments may be caused by dispersion of the spall-induced compression front as it travels through material that has been

somewhat damaged or plastically deformed by the applied tension.

Conclusion

The spall strength of an epoxy–CNT composite and its neat epoxy matrix was measured for a variety of loading profiles using plate impact experiments. The addition of CNTs to the epoxy matrix resulted in a significant reduction in spall strength, which was attributed to the weak epoxy–CNT interface providing nucleation sites for fracture. SEM images of the epoxy–CNT fracture surface indicated that nanotube pullout, due to loss of adhesion at the CNT–matrix interface, was the likely failure mechanism. The neat epoxy showed an important increase in spall strength with increasing incident shock stress that was not observed in the epoxy–CNT composite. This provided further evidence of contrasting spall initiation mechanisms caused by the presence of CNTs.

Acknowledgements The authors would like to acknowledge financial support from the National Research Council Canada (NRC) through the Security Materials Technology (SMT) program and thank A. Higgins for his assistance with the experimental facility and useful feedback on the manuscript.

Funding Funding was provided by National Research Council Canada (Grant No. 859482).

References

1. Grujicic M, Pandurangan B, Angstadt DC, Koudela KL, Cheeseman BA (2007) Ballistic-performance optimization of a hybrid carbon-nanotube/e-glass reinforced poly-vinyl-ester-epoxy-matrix composite armor. J Mater Sci 42:5347–5359
2. Pandya KS, Akella K, Joshi M, Naik NK (2012) Ballistic impact behavior of carbon nanotube and nanosilica dispersed resin and composites. J Appl Phys 112(11):113522
3. Sutherland HJ, Munson DE (1976) Stress wave propagation in a cloth-laminate carbon phenolic. J Compos Mater 10(2):118–128
4. Dandekar D, Boteler J, Beaulieu P (1998) Elastic constants and delamination strength of a glass-fiber-reinforced polymer composite. Compos Sci Technol 58(9):1397–1403
5. Zaretsky E, DeBotton G, Perl M (2004) The response of a glass fibers reinforced epoxy composite to an impact loading. Int J Solids Struct 41(2):569–584
6. Millett JCF, Meziere YJE, Bourne NK (2007) The response to shock loading of a glass-fibreepoxy composite: effects of fibre orientation to the loading axis. J Phys D 40(17):5358
7. Tang L, Zhang H, Han J, Wu X, Zhang Z (2011) Fracture mechanisms of epoxy filled with ozone functionalized multi-wall carbon nanotubes. Compos Sci Technol 72(1):7–13
8. Tessema A, Mitchell W, Koohbor B, Ravindran S, Van Tooren M, Kidane A (2018) The effect of nano-fillers on the in-plane and interlaminar shear properties of carbon fiber reinforced composite. J Dyn Behav Mater 4:296–307
9. Thostenson ET, Ren Z, Chou TW (2001) Advances in the science and technology of carbon nanotubes and their composites: a review. Compos Sci Technol 61(13):1899–1912
10. Rahmat P, Hubert M (2011) Carbon nanotubepolymer interactions in nanocomposites: a review. Compos Sci Technol 72(1):72–84
11. Zhu J, Peng H, Rodriguez-Macias F, Margrave J, Khabashesku V, Imam A, Lozano K, Barrera E (2004) Reinforcing epoxy polymer composites through covalent integration of functionalized nanotubes. Adv Funct Mater 14(7):643–648
12. Spitalsky Z, Tasis D, Papagelis K, Galiotis C (2010) Carbon nanotubepolymer composites: chemistry, processing, mechanical and electrical properties. Prog Polym Sci 35(3):357–401
13. Bie BX, Han J-H, Lu L, Zhou XM, Qi ML, Zhang Z, Luo SN (2015) Dynamic fracture of carbon nanotube/epoxy composites under high strain-rate loading. Composites A 68:282–288
14. Antoun T, Seaman L, Curran DR, Kanel GI, Razorenov SV, Utkin AV (2003) Spall fracture, 1st edn. Springer, New York
15. Curran DR, Shockey DA, Seaman L (1973) Dynamic fracture criteria for a polycarbonate. J Appl Phys 44(9):4025–4038
16. Golubev VK, Novikov SA, Sobolev YS (1982) Effect of temperature on spall of polymeric materials. J Appl Mechan Techn Phys 23:134–141
17. Pepper JE, Huneault J, Rahmat M, Ashrafi B, Petel OE (2018) The effect of curing agent on the dynamic tensile failure of an epoxy subjected to plate impact. Int J Impact Eng 113:203–211
18. Yuan F, Tsai L, Prakash V, Rajendran AM, Dandekar DP (2007) Spall strength of glass fiber reinforced polymer composites. Int J Solids Struct 44(24):7731–7747
19. Katz S, Zaretsky E, Grossman E, Wagner H (2009) Dynamic tensile strength of organic fiber-reinforced epoxy micro-composites. Compos Sci Technol 69(7):1250–1255
20. Curran D, Seaman L, Shockey D (1987) Dynamic failure of solids. Phys Rep 147(5):253–388
21. Pedrazas NA, Worthington DL, Dalton DA, Sherek PA, Steuck SP, Quevedo HJ, Bernstein AC, Taleff EM, Ditmire T (2012) Effects of microstructure and composition on spall fracture in aluminum. Mater Sci Eng A 536:117–123
22. Williams C, Chen C, Ramesh K, Dandekar D (2014) On the shock stress, substructure evolution, and spall response of commercially pure 1100-o aluminum. Mater Sci Eng A 618:596–604
23. Marsh SP (1980) LASL shock hugoniot data. Univerisity of California Press, Berkeley
24. Carter W, Marsh SP (1995) Hugoniot equation of state of polymers (technical report). Los Alamos National Laboratory, Los Alamos
25. Strand OT, Goosman DR, Martinez C, Whitworth TL, Kuhlow WW (2006) Compact system for high-speed velocimetry using heterodyne techniques. Rev Sci Instrum 77(8):083108
26. Cooper PW (2002) Explosives engineering, 4th edn. Wiley, New York
27. Munson DE, May RP (1972) Dynamically determined high-pressure compressibilities of three epoxy resin systems. J Appl Phys 43(3):962–971
28. Petel OE, Jetté FX (2010) Comparison of methods for calculating the shock hugoniot of mixtures. Shock Waves 20:73–83
29. Stepanov GV (1976) Spall fracture of metals by elastic-plastic loading waves. Probl Prochnosti 8:66–70
30. Liu L, Wagner HD (2005) Rubbery and glassy epoxy resins reinforced with carbon nanotubes. Compos Sci Technol 65(11):1861–1868
31. Rahmat M, Das K, Hubert P (2011) Interaction stresses in carbon nanotubepolymer nanocomposites. ACS Appl Mater Interfaces 3(9):3425–3431
32. Wright T, Ramesh K (2008) Dynamic void nucleation and growth in solids: a self-consistent statistical theory. J Mechan Phys Solids 56(2):336–359
33. Wilkerson JW, Ramesh KT (2016) Unraveling the anomalous grain size dependence of cavitation. Phys Rev Lett 117:215503

34. Peralta P, DiGiacomo S, Hashemian S, Luo S-N, Paisley D, Dickerson R, Loomis E, Byler D, Mcclellan K, D'Armas H (2009) Characterization of incipient spall damage in shocked copper multicrystals. Int J Damage Mechan 18(4):393–413
35. Utkin AV, Sosikov VA (2005) Impulsive tension of ethanol under shock loading. J Appl Mechan Techn Phys 46:481–488
36. Grady DE (1988) The spall strength of condensed matter. J Mech Phys Solids 36(3):353–384
37. Utkin AV (2011) Effect of material fracture kinetics on the spalling pulse amplitude. J Appl Mechan Techn Phys 52:151
38. Kanel GI (2010) Spall fracture: methodological aspects, mechanisms and governing factors. Int J Fract 163:173–191
39. Koller DD, Hixson RS, Gray GT, Rigg PA, Addessio LB, Cerreta EK, Maestas JD, Yablinsky CA (2005) Influence of shock-wave profile shape on dynamically induced damage in high-purity copper. J Appl Phys 98(10):103518
40. Gray GT, Bourne NK, Henrie BL (2007) On the influence of loading profile upon the tensile failure of stainless steel. J Appl Phys 101(9):093507